Rapid Thermal Modulation Ion Spectrometry (RTMIS)

Part 1

Underlying Separation Principles and Model of Operation

*Ashley Wilks, Matthew Hart, John Somerville, Andrew Kohel, David Ruiz-Alonso, Paul Boyle, Jon Pearson, Max Allsworth, Alistair Taylor & Lara Jamieson

* Corresponding Author

Owlstone Inc., 761 Main Avenue, Norwalk, CT 06851, Tel: 203-908-4848, e-mail: ashley.wilks@owlstoneinc.com

Abstract

This Technical White Paper essays the fundamental chemical separation and identification mechanisms of Rapid Thermal Modulation Ion Spectrometry (RTMIS). RTMIS is a new technology with roots in Ion Mobility Spectrometry (IMS) and its variants (*e.g.* Differential Mobility Spectrometry and Field Asymmetric Ion Mobility Spectrometry). The clear differentiator of RTMIS from IMS (and its variants) is that RTMIS operates over extreme (and rapidly variable) Electric Field ranges (0 to >75kV. cm^{-1}, 0 to > ~320Td at 1atm). In this regime *Effective Ion Temperatures* may be modulated from ambient to in excess of 1500K. This extreme thermal modulation enables a controlled manipulation (or switching) of the ion chemistry *within* the separation channel (the ion drift region). For example, fragmentation *via* thermal dissociation can be induced. Chemical separation and identification is thus derived from the unique kinetic and thermodynamic behavior of ions assessed over a very broad effective temperature range. This paper thereby draws attention to the aspects of RTMIS, which render it distinct from traditional Ion Mobility technologies and principles, by essaying a model of operation, highlighting model deviations, and providing clear theoretical explanation and experimental evidence.

1 Introduction

Since 2004 Owlstone Inc. has been developing ion separation technologies for use in widely varying chemical detection and identification applications. The result of this effort has been the realization of what we now can show to be an entirely novel Chemical Detection Technology for which we have adopted the title *Rapid Thermal Modulation Ion Spectrometry* (RTMIS). The key breakthrough in technology realization has been the ability to drive a novel design of Differential Mobility / Field Asymmetric Ion Mobility Spectrometer, at extremely high (Ultra-High) fields (>75kV.cm^{-1}, >320Td at 1atm). In the early days of development the effects of operating an ion separation system at the Ultra-High fields enabled by our hardware configuration were not fully understood. It was believed that models applicable to Differential Mobility Spectrometry (DMS) / Field Asymmetric Ion Mobility Spectrometry (FAIMS) would extend to Ultra-High Fields and be sufficient for spectral prediction / interpretation. Detailed data analysis and theoretical work has since revealed that that traditional DMS / FAIMS models breakdown at Ultra-High fields; in particular the α-function approximation is no longer effective. This is largely due to the extremely high *Effective Ion Temperatures* generated at Ultra-High Fields (a result of the strongly non-linear dependence of effective ion temperature on electric field).

On the basis of our up to date understanding, neither DMS nor FAIMS terminology adequately represents the technology, or separation principles when operating at Ultra-High fields. It is for this reason that it has become necessary to isolate the technique and adopt the more representative RTMIS terminology. Ion Kinetics and Thermodynamics *within* the ion filter are fundamental drivers in the separation and identification process and are manipulated by a rapidly scanning Electric Field. The scanning electric field enables effective ion temperatures to be evaluated from ambient to >1500K on single second timescales. Chemical separation and identification is ultimately derived from the unique kinetic and thermodynamic behavior of an ion that is generated from the analytical sample. Specifically, information relating to the *Field Dependent Mobility* and *Fragmentation Pattern* of individual ions is extracted and utilized in chemical classification.

In introducing the RTMIS mode of operation it is necessary to start with a discussion of the principles of Electric Field based gas phase ion separations and in particular the well-established concept of *Ion Mobility* in a neutral drift gas. RTMIS utilizes an oscillating electric field and does therefore have parallels with conventional DMS/ FAIMS at lower applied fields (<35kV.cm^{-1}, ~150Td at 1 atm.). It is thus useful to provide an overview of DMS / FAIMS based separation principles before expanding the discussion to incorporate the principles and differentiators associated with Ultra-High operation and ultimately define the model of operation unique to RTMIS.

1.1 Foundations

Under standard conditions (101.3kPa and 273K) and in a *Low Electric Field* (<5kV.cm^{-1}) the mobility coefficient (K, $m^2.V^{-1}.s^{-1}$) of a singularly charged ion, in a neutral drift gas, is principally governed by its reduced mass μ (kg) and collisional cross section Ω (m^2). K can be *approximated* by the Mason-Shramp equation (Equation 1), where e, is the elementary charge constant (~1.602 x 10^{-19}C), T_{eff} is

the gas temperature (K), k_b is the Boltzmann constant (J.K^{-1}) and N is the molecular density of neutrals in the gas (the drift gas) supporting the ion (2.69 x 10^{25}m^{-3}) [1].

$$K = \frac{3e}{16N} \cdot \left(\frac{2\pi}{\mu k_b T}\right)^{\frac{1}{2}} \cdot \frac{1}{\Omega} \tag{1}$$

Under increasing (but *sub*-Ultra-High) field conditions the local temperature (or *Effective Temperature – T_{eff}*) of the ion begins to rise and can no longer be approximated to the gas temperature. With this increase in temperature the cluster ion is modified, it may expand (*via* the thermal population of rotationally and vibrational excited states) or contract (through the loss of a neutral entity, *e.g.* a weakly dipole or induced dipole bound *solvent* molecule derived from the drift gas) leading to a modification of the collisional cross-section parameter (Ω). At these higher applied fields, Ω is replaced by the *Effective Ion Temperature* dependent collisional cross-section parameter (Ω (T_{eff})) and the gas temperature T by T_{eff} (Equation 2).

$$K(T_{eff}) \approx \frac{3e}{16N} \cdot \left(\frac{2\pi}{\mu k_b T_{eff}}\right)^{\frac{1}{2}} \cdot \frac{1}{\Omega(T_{eff})} \tag{2}$$

At constant N (*i.e.* gas constant pressure) the mobility coefficient K is thereby Electric Field dependent by virtue of the influence of the Electric Field on T_{eff} and K is therefore molecular specific on the basis of its dependence on Ω. This phenomenon is exploited for molecular separation and identification in DMS / FAIMS based systems. By passing an ionized gas through the gap between a pair of electrodes over which an oscillating *asymmetric* electric field is applied the mobility of the ion will oscillate between a low field mobility $K(0)$, which may be approximated to be representative of the *Reduced Mobility Coefficient (K_0)* (*i.e. the mobility in at an applied field of low magnitude, where $T_{eff} \approx T$*) and a high field mobility $K(E)$ (Figure 1). The change in K occurring in the high field portion of the asymmetric waveform is a result of the high field influence on T_{eff} and Ω (T_{eff}).
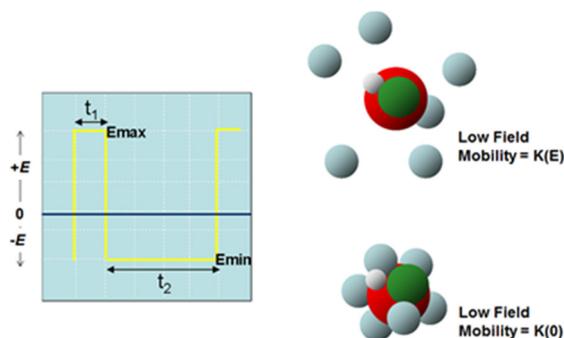

Figure 1: In an oscillating electric field the mobility of an ion will oscillate between a low field mobility ($K(0)$) and a high field mobility ($K(E)$) [2]. The differential mobility ($K(0) – K(E)$) may be positive or negative in sign, depending whether there is an increase or decrease in Ω as a result of the *Field Heating* effect.

1.2 Field Dependence of *K*

At Standard Temperature and Pressure (STP) the field dependency of $K(E)$, *to an* **approximation** over a **moderate field range** (~0 – 30 kV.cm^{-1}), may be related to the low field mobility

$K(0)$, through *Equation 3*, whereby α is the function of the $K(E)/K(0)$ versus E curve [2 & 3].

$$K(E) = K(0)[1 + \alpha(E)] \tag{3}$$

The α-function is polynomial expandable in even powers (*Equation 4*), where the coefficients α_1, $\alpha_2...\alpha_n$, are specific to the ion, and more importantly the parent molecule (or molecular fragment) forming the ion.

$$K(E) = K(0) [1 + \alpha_1 E^2 + \alpha_2 E^4 ... + \alpha_n E^{2n}] \tag{4}$$

The high order terms can usually be neglected since they are of diminishing significance (in the realms of experimental precision) and *Equation 4* can be truncated to the fourth order -

$$K(E) = K(0) [1 + \alpha_1 E^2 + \alpha_2 E^4] \tag{5}$$

Since DMS / FAIMS systems utilize a non-perfect square waveform to drive the oscillating field, it is extremely important that E is accurately defined. E is the **zero** to **peak** amplitude of the electric field generated by a waveform of zero to peak voltage (V) across electrodes of gap separation g (cm^{-1}). This is referred to as the Dispersion Field – E_D (kV.cm^{-1}).
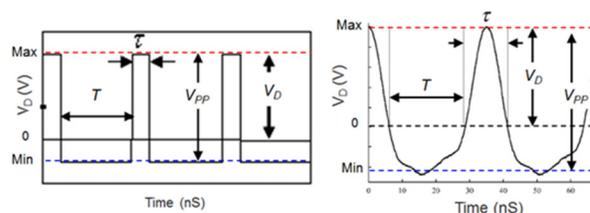

Figure 2: Idealized square rectangular waveform (left) and approximation of actual waveform (right), utilized in RTMIS separations. The Dispersion Field strength (E_D) is defined by the zero to peak voltage of the applied waveform (V_D) across the electrodes that form the ion filter (Figure 4).

This variable field definition is very important since the assumption that $K(0)$ is representative of the low field mobility does not hold up well at very high fields (where the field across the separation electrodes will actually be significant in the "low field" portion of the applied asymmetric field). This is one of the aspects of RTMIS that distinguishes it from variants of FAIMS / DMS, which operate over a much lower range of E_D (~ 0 – 35 kV.cm^{-1} *c.f.*, 0 - 75kV.cm^{-1}) and absolutely stresses the approximations of Equation 5. We shall go on to discuss throughout this paper.

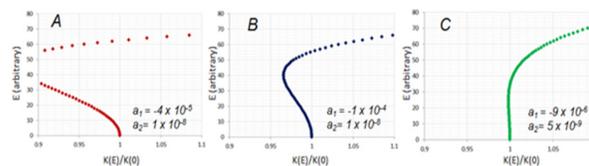**Figure 3:** K(E)/K(0) = 1 + α(E) for a series of a_1 and a_2 coefficients.

The a-coefficients in *Equation 5* are very small relative to E (~10^{-5}, ~10^{-9} respectively) and may be *Positive* or *Negative* in sign. The ratio $K(E)/K(0)$ may therefore be > 1 or <1, reflecting the fact that the high field mobility K(E) may be less than, or greater than, the low field mobility at various points across the $K(E)/K(0)$ *versus E*

curve (Figure 3). By the same token we can say that ΔK (defined as $K(E) - K(0)$) is positive in sign when the high field mobility exceeds the low field mobility and negative in sign when the opposite is the case. For low and medium molecular weight species (*e.g.* volatile chemical threats) ΔK will typically range some 0 to 10% of the low field mobility ($K(0)$) and this should be kept in mind (*i.e.* the Differential Mobility is *small* relative to low or high field mobility). In modeling performance it is difficult to precisely define $K(E)$ and as a result *approximation* usually needs to be made in which $K(E)$ is approximated to $K(0)$ (or more specifically K_0 – the *normalized reduced mobility co-efficient*), for which a plethora of data tables exist for volatile chemical threats.

In *rough* terms, a positive ΔK is observed when the ion "shrinks" (*i.e.* the Ω decreases) on the transition between the low field and high field portion E_D, while a negative ΔK is observed when the ion "expands" (*i.e.* Ω increases) on the transition. The *(T_{eff})* function is very nonlinear and is dependent on a variety of molecular specific physical and chemical properties (*e.g.* ion clustering / declustering kinetics and the efficiency of energy transfer during ion-neutral molecular collisions). As such, the *sign* of ΔK can change with increasing E_D (Figure 3).

1.3 Separation Mechanism

Post ionization, ions are transported transverse (perpendicular to the applied field) through the separator electrodes in a uniform gas flow. At constant E_D the ΔK induced by the oscillating asymmetric field manifests as alternation of the longitudinal (parallel to the field) drift velocity (v_D, cm.s^{-1}) between the high field portion of the applied waveform (of a duration τ, s) and low field portion of the applied waveform (of a duration T, s). This is illustrated in Figure 4.
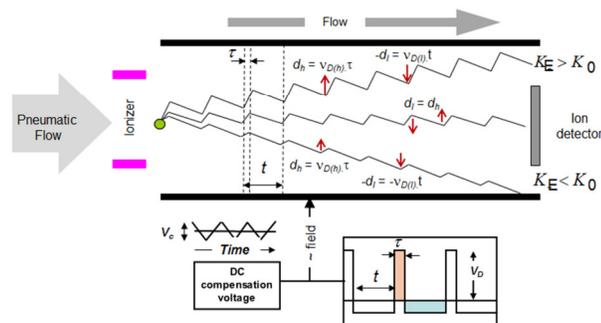

Figure 4: Ion Drift in an oscillating electric field as employed in RTMIS. A variable high voltage asymmetric waveform of low voltage pulse duration T (s) and high voltage duration τ (s) and peak voltage V_D is applied between electrodes of gap g (cm), creating a variable Field of V_D / g (kV.cm^{-1}), through which ions oscillate and adopt a net longitudinal drift path length ($d_h - d_l$), which is determined by their high and low field drift velocity ($v_{D(h)}$ and $v_{D(l)}$) and the high / low pulse duration. A bias DC "tuning voltage" (V_c) applied on top of the applied waveform enables subtle adjustment of V_D to counter the drift experienced by an ion of a specific ΔK.

The longitudinal drift velocity is given by the relation $v_D = K.E$. When $K(E) > K(0)$, v_D will be higher (and the longitudinal distance covered by the ion greater) in the high field portion of the applied waveform, while it will be lower (and the longitudinal distance covered by the ion lesser) in the low field portion of the applied waveform. When $K(E) < K(0)$ the converse will apply. Simply, the direction of the longitudinal drift will depend on the sign of ΔK; the

net drift being in the direction of the top separator electrode when ΔK is positive in sign and toward the bottom electrode when ΔK is negative in sign. At a given E_D, only ions of $\Delta K = 0$, or else those whose drift velocities are matched such that the longitudinal high field drift path length d_h (cm) is equal to the longitudinal low field drift path length d_l (*through the relation $d_h = v_{D(h)}.\tau$ and $d_l = v_{D(l)}.t$, where $v_{D(h)}$ are $v_{D(l)}$ are the respective high and low field drift velocities*), will be carried fully parallel to the gas flow and detected. Other ions will be neutralized on the separator electrodes. Clearly, the condition where $\Delta K = 0$ (*i.e. $K(E)/K(0) = 1$*) is very precisely field dependent (as Figure 2 illustrates) and only true at relatively high, or else very low, E_D. Nevertheless, *subtly* tuning E_C (~± 5%) around a given E_D set point will be sufficient to offset any net longitudinal drift experienced by an ion of a given ΔK. This tuning field is referred to as the Compensation Field (E_C) and in sweeping E_C, ions are selectively filtered on the basis of their ΔK. Further, since ΔK exhibits molecular specificity and is a strong function of E_D, the ion current output obtained when stepping E_D in combination with a sweeping E_C offers a highly molecular selective output. The RTMIS $E_C:E_D$ output is the Dispersion Spectrum that is also synonymous with DMS / FAIMS technologies.
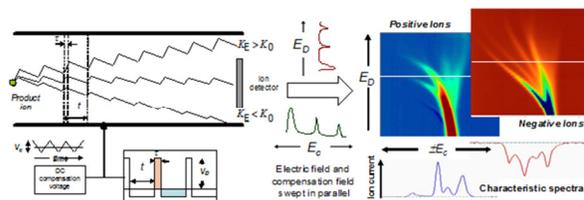

Figure 5: Schematic of the ion separation principle in RTIMS. The V_C applied across the electrode of gap g manifests as the *Compensation Field* (E_C - kV.cm^{-1}) and V_D the *Dispersion Field* (E_D - kV.cm^{-1}). Since ΔK is field dependent, the stepping of E_D in combination with a sweeping E_C provides a quasi-orthogonal output for high confidence chemical classification. The selective ion filtering can deliver very high speed (sub-second) chemical separation and identification capability.

1.3.1 Standardization of Electric Field to *E/N*

The mobility co-efficient K is pressure dependent by virtue of the $1/N$ dependency in Equations 1 and 2. Normalization with respect to pressure is therefore essential to overcome the effects of natural meteorological variation and E (V.m^{-1}) is replaced with E/N (V.m^2). At STP (101.3kPa and 295.15K) N (m^{-3}) is very large (2.503 x 10^{25} m^{-3}) and *E/N* and very small (~10^{-19} V.m^2 at E = 200kV.cm^{-1} under the same STP condition). A more convenient unit in *E/N* expression, for spectral representation, is the Townsend (Td), where 1 Td = 10^{-21} V.m^2) [4].

1.4 Logistics of Ultra-High Field Operation

Operation at Ultra-High fields requires the use of very narrow gap (micron-scale) ion filters, in order to relax the engineering challenges associated with waveform driver design. Minimizing the ion filter gap ultimately enables higher fields to be generated with lower voltage and smaller form-factor waveform drivers (Figure 6). That said waveform driver development requires an exceptional appreciation for magnetic circuit design. The development of high voltage, high frequency asymmetric waveforms, with a "size and power" optimized topology, has been a beyond state-of-the-art exercise.
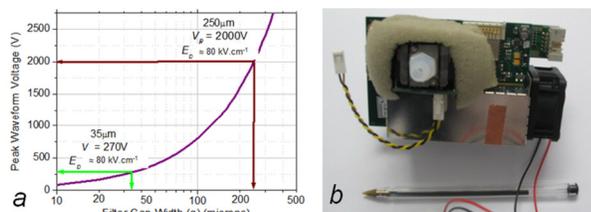
Figure 6: The Practical and physical advantages of reducing the filter gap (*g*) in FAIMS. (a) Higher peak fields can be generated with a much lower peak voltage and hence a more efficient, smaller form-factor electronic driver. b) Present generation (OEM) RTMIS RF drive stage integrated with DC drivers and RTMIS sensor head assembly.
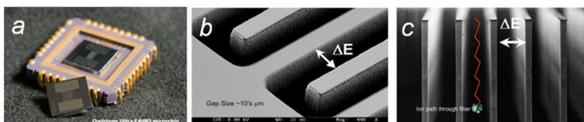

Figure 7: Inter-digitated micro-fabricated ion separator for Ultra-High Field operation [5]. a) Etched ion filter in sensor package, b) Magnification of sensor surface showing serpentine ion filter channels, c) Simulation of cross-section through senor showing parallel filter channel arrangement (with schematic of ion passing through a channel overlaid where ΔE denotes the applied field).

Use of such narrow gaps also warrants the use of short ion separation channels and substantially higher asymmetric waveform frequencies, as compared to those employed in macro-gap designs (300μm *c.f.* 1cm and 27MHz *c.f.* 1MHz respectively). Short ion separation channels must be employed in order to maximize ion transmission and high waveform frequencies must be employed such that a sufficient number of ion oscillations may occur (in a short ion filter channel) to promote ion separation. The combination of high frequency and short channels means that ion-molecule collisions are minimized in LF and HF period of the applied waveform (between which, ion chemistry is manipulated) as well as in the short timescale (μs) transit through the channel (Figure 8). This has profound effects on ion chemistry, since separation timescales become more comparable to natural ion-neutral collision frequencies at atmospheric pressure (~5GHz). Short-lived ion fragments generated *within* the ion filter may therefore be observed and utilized in classification, as we shall go onto see later in this paper.
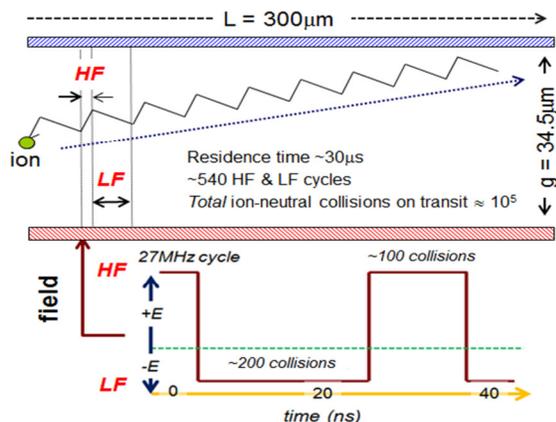

Figure 8: Schematic representing ion transport through the ion filter. Ion-neutral collisions (of ~5GHz in frequency) during each high and low field cycle, at operational pressure (1atm), are relatively few.

2 Instrumental Specifics

The ion filter (Figure 7) consists of 27 ion channels of gap width (g) = 34.5 (±0.2) μm and length (L) = 300 (±0.2) μm. It is fabricated by etching a 37mm long serpentine channel into a silicon wafer to form a 1.2mm^2 open area. The gap surfaces are made of high-conductivity silicon and are electrically connected *via* wire bonding to metal pads on the face of the silicon. The chip is packaged and mounted onto a bespoke high-temperature co-fired ceramic (HTCC) package.

The asymmetric waveform is synthesized using a proprietary Radio Frequency (RF) circuit design. The RF output contains significant higher order terms but can be approximated by 2 sinusoids - a fundamental and its first harmonic. The first harmonic is $^1/_2$ the amplitude of fundamental and 90° out of phase, yielding a waveform of the function.

$$V(t) = \sin(\omega_1) + 0.5\cos(2\omega_2) \qquad (6)$$

Where ω_1 and ω_2 are the angular frequencies of the fundamental and first harmonic (Hz) and *V* is the voltage (V). A digital oscilloscope recording of the waveform as applied across the ion filter electrodes is shown in Figure 9.
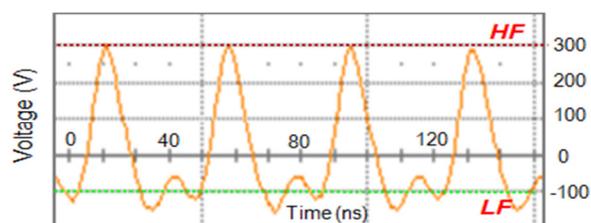

Figure 9: Digital Oscilloscope recording of separation waveform applied across the ion filter at 300V zero to peak voltage (≈ 85.7kV.cm^{-1} and 365Td at 1atm).

The amplitude of the waveform in the high-field segment (Dispersion Voltage) is variable up to ~250V corresponding to a Dispersion Field (E_D) range of 0 – 75kV.cm^{-1} (equivalent to E_D/N = 0 – 320Td under standard atmospheric operational conditions, 101.3kPa). The addressable E_D resolution is 14V/cm corresponding to E_D/N = 61mTd under the same conditions and may be stepped at rates of up to 10 *divisions per second* parallel with the Compensation Field sweep.

The "tuning" *Compensation Field (E_C)* is generated by a DC voltage superimposed on the asymmetric waveform as illustrated in *Figure 4*. The DC voltage may be swept in a range of ±8V with <2mV addressable resolution at a rate of 1.3ms.step^{-1}, yielding an E_C of ±2.3kV.cm^{-1} and <1V.cm^{-1} resolution (equivalent to ± 10Td, with 2mTd resolution under standard atmospheric pressure operational conditions). A sweep of ± 6Td more than adequately suffices (as one approaches maximum E_D/N) for volatile and semi-volatile compounds (MW < 350 AMU).

Ions are carried through the ion filter in air at ambient pressure. The ion source is Owlstone's custom designed corona discharge device (patent pending) that generates both positive and negative ion species. The ion filter may be heated in a range of ambient to 60(±1)°C, and is monitored / stabilized by means of a temperature sensor (Microchip, TC74A5-5.0VAT) in feedback loop with the heater controller. The inlet sample may be diluted in a ratio

ranging from 3:1 to 30:1 in a recirculating dry and purified air flow, whereby the air exiting the ion filter is purified through an activated charcoal and molecular sieve "scrubber" with integrated particulate filter. The standard flow rate through the ion filter is $350(\pm10)cm^3.min^{-1}$ and the sample inlet to diluent flow ratio is controlled by a variable solenoid valve at the outlet of the sensor assembly (where the sensor assembly is defined as an assembly of the ion source, ion filter package, ion detector and ancillary sensing devices, Figure 10). An exhaust solenoid placed in front of the variable solenoid allows for complete air recirculation (*i.e.* shut off of the inlet sample flow) providing protection from contamination scenarios. Air is pulled through the sensor assembly by means of a rotary vane pump. A temperature and pressure sensor (Bosch BMP085) is mounted at the exit of the sensor assembly to accurately monitor the gas temperature and pressure. A humidity and temperature sensor (Sensirion, SHT15) is mounted at the sample inlet to monitor these ambient variables (Figure 11)
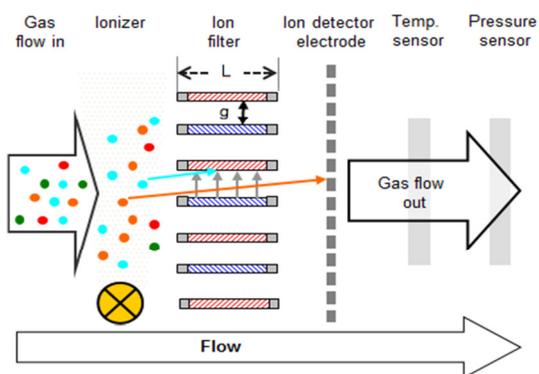

Figure 10: "Sensor head" arrangement. L represents the filter channel length (300μm) and g the filter channel gap (35μm) across which the Dispersion and Compensation Fields are applied.
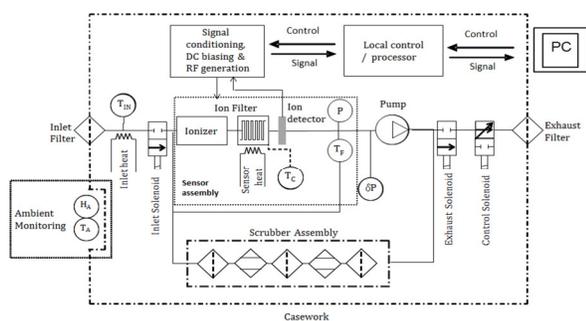

Figure 11: System diagram

The ion detector electrode consists of a gold plated hexagonal grid of 6 x 0.5mm holes positioned 1mm after the chip and biased at ±30V on alternating sweeps of the compensation field for cation and anion detection. The ion current impacting the electrode is measured by a Transimpedance Amplifier (TIA). As standard a E_C sweep time of 420ms with 400 E_C steps, yields a sampling time of approximately 1ms.step^{-1}. Ion current response data is passed to a local processor (ARM 7- TDMI), which serves also to set spectral acquisition parameters (E_C range, E_D range, step size, *etc.*). High-level systems control is performed by a PC (Dell, Latitude E5500), with a custom control / data acquisition user interface, which is

linked by USB to the local processor. This user interface also serves to present spectral data in real time and log data for offline analysis.
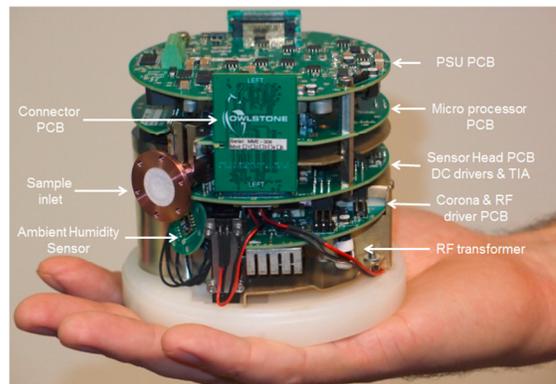

Figure 12: Photograph of Hardware layout

2.1 Separation Waveform Analysis

The generation of a high voltage, high frequency asymmetric waveform is non-trivial. RF circuits are inherently non-linear, so the separation waveform applied across the ion separator must be well characterized through the operational field range. The waveform employed by the authors closely matches the sum of 2 sinusoids described by Equation 6 but is non-ideal. The peak waveform voltage is not a linear function of the bias applied to the RF oscillator (*or, more specifically, the equivalent circuit formed by the RF circuit coupled to the ion separator*) and the precise function of the waveform exhibits some dependence on this bias voltage. Comparisons against a FAIMS / DMS model can only be made with clear quantification of critical waveform parameters through the operational field range. These critical parameters are; *i*) the power (and thus *V*) transfer function ($V_p(V_b)$) , *ii*) the peak voltage *vs.* frequency response ($\omega(V_p)$) and *iii*) the precise function of the waveform (*f(t)*). The importance of *i*) is automatically realized through inspection of Equation 3 and the importance of *ii*) can be rationalized (when considering also the ratio of HF and LF period) in terms of its impact on ion kinetics in the HF and LF segment of the applied waveform. The importance of *iii*) is less straightforward but a mathematical description has been widely discussed (*e.g.*, [6]). This description reduces the separation waveform to a series of coefficients which help define the $E_C{:}E_D$ spectrum for a given ion, in a separation field derived from a waveform of function *f(t)*. The waveform coefficients are defined as -

$$\langle f_n \rangle = 1/T \int_0^T f_n(t)dt \qquad (7)$$

where *T* is the period of the waveform, *i.e.*, $t + \tau$ in Figure 4. In the field dependence of ion mobility approximated by Equation 4 the lower order coefficients $<f_2>$, $<f_3>$ and $<f_5>$ are of specific importance.

All critical waveform parameters have been evaluated through assessment of the waveform as measured across individual channels on the multi-channel ion separator. The waveform was recorded at a range of oscillator bias voltages using a high sample rate digital storage oscilloscope (and independently across three of

the 27 channels separation; *channels 1, 12* and *20*) using an impedance matched coupling probe. The peak and minimum waveform voltages, as a function of the bias voltage, were then derived to obtain the bias voltage transfer function before subsequently deriving the separation waveform coefficients $<f^2>$, $<f^3>$ and $<f^5>$ and also the $\omega(V_p)$ dependencies. The data is summarized in Figures 13 and 14.
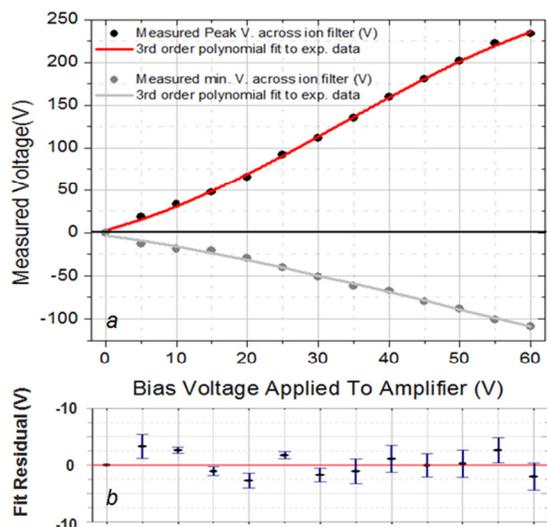

Figure 13: a) Measured peak and minimum (*i.e.*, absolute minimum accounting for measured deviation from Equation 6) waveform voltages as a function of oscillator bias voltage. The peak and minimum voltage transfer functions closely fits a 3rd order polynomial, $y = a + bx + cx^2 + dx^3$, where constant a is fixed to 0V ($R^2 > 0.999$). b) Residual data (obs – fitted) for the **peak** waveform voltage, where error bars are the standard deviation for each measurement across channels 1, 13 and 20 on the ion separator.
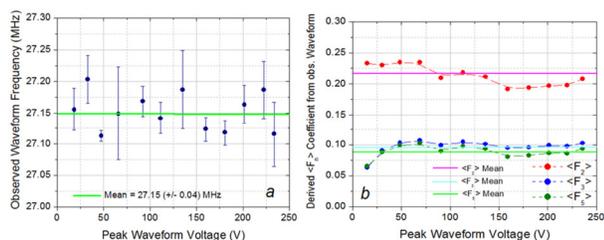

Figure 14: a) Measured Waveform frequencies across peak waveform voltage range (uncertainties represent standard deviations, n = 3). b) Waveform coefficients $<f_2>$, $<f_3>$ and $<f_5>$ across peak waveform voltage range derived from the observed waveform, noting that errors for n = 3 measurements relating each peak waveform voltage point were <0.005 (*i.e.* <5% RSD)).

The $V_P(V_b)$ response (Figure 12) could be closely approximated to a cubic function, with measurement uncertainties scaling roughly with V_b. These were ~±2.5% RSD, except at the lowest V_b setting at which measurements were taken, where an RSD of ~±10% was observed. It is to be noted that accuracy in V_p is less critical at the very low end of the scale since at low E_D/N (<25Td) RTMIS peaks are only partially resolved. We could conclude then that the V_p of the waveform was quantitatively characterized for precise E_D/N scaling.

The $\omega(V_p)$ response (Figure 14a) was effectively constant (given measurement uncertainties) across the working V_p range. Taking the mean of all measurements we defined the waveform frequency as 27.15 (±0.04) MHz. More interesting were the derived $<f_n>$ waveform coefficients, which account for departures of the waveform function from Equation 6 (due to the presence of higher order terms). The coefficients were well defined at any single V_p but varied across the working V_p range. These coefficients ranged from 0.1918 – 0.2348, 0.0634 – 0.1073 and 0.0654 – 0.1052, for $<f_2>$, $<f_3>$ and $<f_5>$ respectively. At the minimum V_p measurement point the measured $<f_3>$ and $<f_5>$ coefficients deviated most from the mean values and these points were dropped from the final mean $<f_n>$ calculations. The $<f_2>$, $<f_3>$ and $<f_5>$ coefficients were thereby defined as 0.2134 (±0.0160), 0.0967 (±0.0048) and 0.0879 (±0.0070). The validity of using averaged across operation field range $<f_n>$ values in spectral evaluations is addressed in Section 3.1.

2.2   Definition of Ion Residence Time (t_{res})

A firm definition of the ion residence time within the ion channel is required in order to perform effective systems validation. The gas flow through the ion channel is Laminar (parabolic). Ions are only detected when $v_{D(h)} = v_{D(l)}$ (*c.f.* Figure 4) and these ions emanate from the center of the ion channel. Under a laminar flow condition the maximum flow velocity (v_{max}, m.s^{-1}) occurs at the center of the ion channel, whilst the minimum flow (v_{max}) velocity occurs at the edges. The average flow velocity (v_{Av}) is defined as Q/A, where Q is the gas flow rate (m^3.s^{-1}) and A the surface area of open flow channels (m^2). In a macro-circular channel v_{max} under a laminar flow condition is easily defined by the expression $2Q/A$. For a rectangular (planar) micro-channel, however this relationship does not hold. Indeed the accurate determination of V_{max} is an involved process [7]. A reasonable approximation can nevertheless be made by integrating the equation which defines the flow velocity (v_x) at any point (x), between the extremes ±x, through the cross section of the ion channel; $v_x = v_{max}(1-x^2)$. Doing so one derives the expression $v_{max} = {}^3/_2 . v_{Av}$, *i.e.*, the maximum flow velocity defining t_{res} is 1.5 that of the average flow velocity and t_{res} is given by the expression –

$$t_{res} = L.A/(3Q/2) \tag{8}$$

Based on our open channel area of 1.17mm^2, channel length of 300μm and a typical operational flow rate of 350 - 400cm^3.s^{-1} this yields an ion residence time of ~30 - 40μs.

3   Model of Operation

The spectral output (the Dispersion Spectrum) is analogous to that observed in conventional DMS / FAIMS in so far as it consists of an m x n matrix of ion current measurements at m Compensation Field (E_C/N) and n Dispersion Field (E_D/N) settings (Figure 12). A spectral peak at fixed E_D/N can be characterized by its Gaussian parameters, *i.e.*, position (E_C/N), height (I) and width (w). The $E_C{:}E_D$ spectrum, which is the evolution of Gaussian response as a function of E_D/N, can be characterized by the derived Gaussian parameters. A dense $E_C{:}E_D$ spectrum may be obtained on single second timescales because ion separation times are short (~30μs). The $E_C{:}E_D$ spectrum is viewed holistically in deriving information

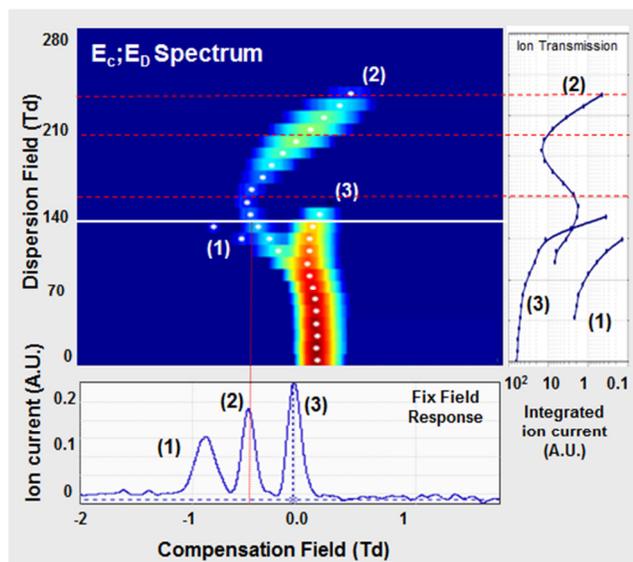about the analyzed sample and performing agent classification (Figure 15).

Figure 15: The E_C:E_D spectrum represents the ion current at the output of the Ion filter as a function of the Compensation Field (E_C) and the Dispersion Field (E_D). The Ion Transmission spectrum represents the integrated Ion current for each resolved peak as a function of E_D.

In discussing the model of operation it is helpful to establish a foundation based on the DMS / FAIMS model and then to build upon this. DMS / FAIMS models are well established and provide an invaluable starting point in the lead up to the discussion of Ultra-High Field operation. The work of and Shvartsburg [3], Krylov *et al.* [6] and Guevremont [8] is fundamental in the discussion that follows.

3.1 Ion Peak Position

At lower E_D/N (<140Td) it may be shown that the peak position (E_C/N) may be *approximated* by considering the field dependency of the ion mobility coefficient (α, *Equation 5*) and the Dispersion Field amplitude (E_D/N) by the relation -

$$E_C / N = c_3 (E_D/N)^3 . c_5 (E_D/N)^5 \qquad (9)$$

in which the constants c_3 and c_5 are given by -

$$c_3 = \alpha_2 \langle f_3 \rangle \qquad (10)$$

$$c_5 = (\alpha_4 \langle f_5 \rangle) - (3c_3 \alpha_2 \langle f_2 \rangle) \qquad (11)$$

and the parameters $<f_2>$, $<f_3>$ and $<f_5>$ are *separation waveform coefficients* dictated by the function of the waveform from which the Dispersion Field is generated. These waveform coefficients were defined, for the waveform employed by the present authors, in Section 2.1. On this basis, a *simulation* of the E_C:E_D spectrum is possible given a knowledge of the α_2 and α_4 parameters of Equation 9. The inverse problem is solvable; *i.e.*, α_2 and α_4 parameters may be derived from a fit of Equation 9 to the empirical spectral data (*c.f.*, Figure 16).
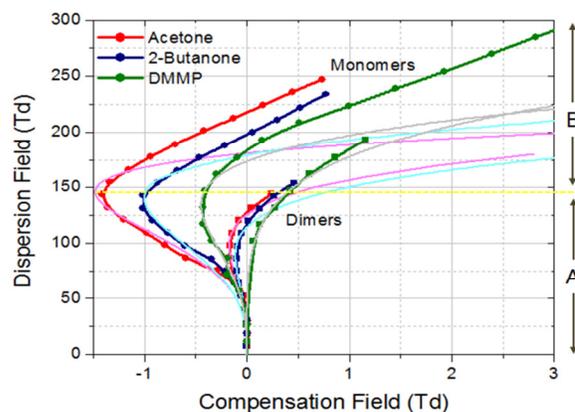

Figure 16: RTM-IS E_C:E_D peak trajectories for monomer and dimers of Acetone, 2-Butanone and Dimethyl, Methyl Phosphonate (DMMP) obtained experimentally (vapor concentrations of <1ppm by volume at <10ppm [H_2O]) and polynomial least squares fits of Equation 9 to lower Dispersion Field data only, (region A). A reasonable fit can be obtained at lower Dispersion Fields enabling α parameters to be extracted. However, at Higher Dispersion Fields (>140kV.cm^{-1}, region B) empirical data no longer fit the α-model (Section 3.1.1).

It may be recalled from Section 2.1 that the waveform coefficients show some deviation across the V_p range. In data evaluation the mean values are used. The validity of this requires consideration, given that the peak position is dependent on these coefficients. To evaluate this we model the E_C:E_D response for the acetone monomer and dimer using the min, mean and maximum values for each of the derived coefficients recorded in Figure 14b (ignoring the data points at $V_p = 11V$). The result is shown in Figure 17. Whilst we do see some offset at any fixed E_D/N, it should be remembered that there is already a marginal uncertainty in the Dispersion Field (~±2%) from the $V_p(V_b)$ transfer function (Figure 13). On this basis, any offset introduced from uncertainties in the waveform coefficients can be considered relatively insignificant.
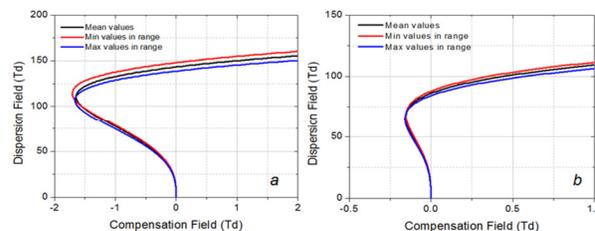

Figure 17: Simulated E_C:E_D responses for the acetone monomer (left) and dimer (right) using the minimum min, mean and maximum values for each of the derived f_n coefficients recorded in Figure 14b. (α_2 and α_4 coefficients were taken from Krylov et al [n].

3.1.1 Alpha-model breakdown

The problem with the α-model is that it is only applicable at lower E_D/N (<150Td) as illustrated in Figure 16. At higher E_D/N the model predicts that the peak E_C/N position → E_D/N, whereas real ions do not behave as such. Appreciation of why this is the case requires a detailed consideration of the ion chemistry within the ion filter, in particular the *kinetic* and *thermodynamic* impacts resulting from the highly non-linear dependency of Effective Ion Temperature (T_{eff}) on E_D/N. We explore this in Section 3.2, which addresses ion transmission and peak intensity.

3.2 Ion Peak Intensity

Understanding the relationship between E_D/N and the Ion peak intensity requires a combined consideration of 1) Ion Transmission through the filter (dictated by the drift gas flow rate, molecular ion diffusion and the combined length / width of the ion filter channel) and 2) Ion chemistry in the ion filter. The former is easier to address since it has been well defined for the *lower field* (DMS / FAIMS) case by Krylov *et al.* [6] and we shall start here.

3.2.1 Lower Field Range (<150Td)

The ion filter we employ is effectively an assembly of 27 parallel planar electrodes. The ion density distribution within the ion filter channels fits the "weak focusing" (planar) case described by Krylov *et al.* [6]. The analysis of Krylov *et al.* rationalizes in terms of peak height, since for the planar ion filter they describe, the peak width could be roughly approximated as independent of E_D/N. In the case of the ion filter described by the present authors the peak width exhibits a dependence on E_D/N (as shall be explained in Section 3.3). As such peak height must be substituted for peak area, (integrated ion current), which is independent of broadening effects encountered across the E_D/N scan range.

The integrated peak ion current (A_I) will be some fraction of the "averaged over cross-section" input integrated peak ion current, $A_{I(in)}$. In the *weak focusing* case A_I may be approximated through the Equation -

$$A_I = A_{I(in)}.Q.\exp\left(-t_{res}.\pi^2.D_{II}\,/\,g_{eff}{}^2\right) \tag{12}$$

where Q is the gas flow rate ($m^3.s^{-1}$), t_{res} the ion residence time in the ion filter (s), D_{II} the *anisotropic* ion diffusion coefficient ($m^2.s^{-1}$) and g_{eff} the effective gap width (m).

g_{eff} is smaller than the physical gap width (g) and corrects for the longitudinal (*parallel to the applied field*) displacement of an ion during a HF (d_H) or LF (d_L) waveform cycle (Figure 4), noting that at the ion peak $d_H = d_L$. Using $g_{eff} = g - d_L$ and (recalling from Section 1) that $d_{(L)} = v_{D(L)}.t$ and $v_{D(L)} = K_{(0)}.E_{min}$, g_{eff} is defined by -

$$g_{eff} = g - (K_{(0)}.E_{min}.t) \tag{13}$$

where E_{min} ($V.m^{-1}$) is the *average* field across the ion filter in the duration of a LF cycle of the Dispersion Field waveform. g_{eff} is thereby proportional to $1/E_{min}$, across the Dispersion Field range. Figure 18 shows that for a typical ion of $K_0 \approx 1.8 \times 10^{-4}$ $m^2.V^{-1}.s^{-1}$, this scales from $g_{eff} = g$ (*i.e.*, 35μm) at $E_D = 0kV.cm^{-1}$, through $g_{eff} \approx$ 25μm at the near maximal E_D of 75kV.cm^{-1} (*i.e.*, $E_{min} \approx$ 18kV.cm^{-1}, based on the waveform described in Equation 6); noting that g_{eff} is strictly dependent on the field strength E ($V.m^{-1}$), as opposed E/N ($V.m^2$).

The other field dependent term in Equation 12 is the *anisotropic* ion diffusion coefficient (D_{II}), which accounts for longitudinal diffusional losses to the ion filter during transit [3]. D_{II} is defined by Equation 14 -

$$D_{II} = D\left[1 + \langle F_2 \rangle F_{II} M K_0{}^2 N_0{}^2 (E_D/N)^2\,/\,(3k_bT)\right] \tag{14}$$

where M is the molecular weight of the drift gas (kg), D is the isotropic diffusion coefficient defined by the Einstein relationship -

$$D = k_bTK_0N_0\,/qN \tag{15}$$

and F_{II} is a property of the ion-neutral molecule potential which may be *approximated* by *Equation 16* (in which m is the molecular weight of the ion). The other terms appearing in Equations 11, 12 and 13 have their previous meanings.

$$F_{II} = 1 + (2m\,/(M + 2m)) \tag{16}$$

Replacing g_{eff} and D_{II} in Equation 12 with an array of outputs from *Equations 13* and *14*, computed for a specific ion species, across the operational $E_D;N$ range, we arrive at the purely physical field dependent transmission behavior of the ion. This is exclusive of consideration of *intra-molecular* and *inter-molecular* ion-ion or ion-neutral interactions. In a theoretical analysis we do this for Acetone, butanone and DMMP (monomers and dimers), as well as the hydrated proton and dioxygen anion (Figure 19). What this reveals is the strong dependency on K_0, which should not be surprising given the appearance of the K_0 term in Equations 13, 14 and 15. The F_{II} contribution embedded in Equation 14 is, by comparison, a negligible factor in determining the transmission behavior since, usually $m \gg M$ and $2m/(M+2m)$ tends to unity.

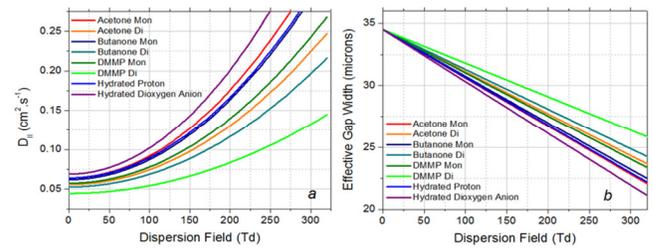**Figure 18**: a) $D_{II}(E_D/N)$ for various product ions of differing K_0 (listed in Table 2) and b) $g_{eff}(E_D/N)$ for the same ions. Computed at 318K (gas temperature) and 101.3kPa.
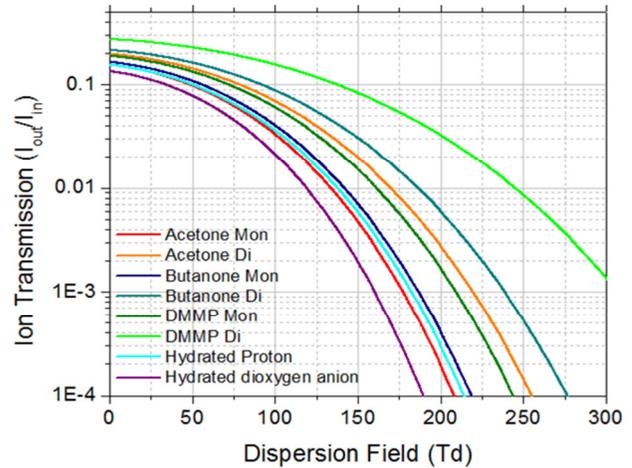

Figure 19: Ion transmission (without consideration of inter and intra-molecular interactions in the ion filter region) for various product ions of differing K_0 (listed in Table 1) at a gas temperature of 318K and pressure of 101.3kPa.

Case	Ion identity	K_0 (cm^2.V.s^{-1})	D (cm^2. s^{-1} x 10^{-2})	F_{II} (unit-less)
Acetone (M)	$(C_3H_6O)H^+.(H_2O)_2$	2.11 [10, 11]	6.24	1.87
Acetone (D)	$(C_3H_6O)_2.H^+$	1.83 [10, 11]	5.44	1.89
Butanone (M)	$(C_4H_8O)H^+.(H_2O)_2$	2.03 [10, 11]	6.03	1.88
Butanone (D)	$(C_4H_8O)_2.H^+$	1.73 [10, 11]	5.14	1.91
DMMP (M)	$(DMMP).H^+(H_2O)_2$	1.88 [12]	5.59	1.92
DMMP (D)	$(DMMP)_2.H^+$	1.46 [12]	4.34	1.95
Hyd. Proton	$H^+.(H_2O)_2$	2.10 [10]	6.24	1.72
Hyd. O$_2$ anion	$O_2^-.(H_2O)$	2.26 [10, 13]	6.72	1.78

Table 1: Molecular constants used in D_{II}, g_{eff} and Ion transmission simulations (Figures 18 and 19). Ion identity is speculated on the basis of a dry (<10ppm$_m$ H$_2$O) air drift gas. These K$_0$ values are carried over to experimental data evaluation in Section 4.

3.2.2 Higher Field Range (>150Td)

At higher E_D/N (>100Td) the above transmission model begins to breakdown. The model does not account for (in particular); the kinetic and thermodynamic aspects of ion behavior within the ion filter, which are driven by the *Field-Heating* effect, where we define Field Heating as the raising of the *Effective Temperature* of the ion to a temperature exceeding its surroundings. Effective Ion Temperatures scales $\sim E_{D/N}^2$ so, as we enter the Ultra-High field operational regime Field-Heating strongly dictates the ion transmission behavior, since ions may dissociate / breakdown forming entities with entirely different K_0 values.

Definition of Effective Ion Temperature

The field heating process is due to the conversion of kinetic energy acquired by ions in the applied field to thermal energy on collision with neutrals. In the absence of an applied field the total energy (E_T, J) of the ions and neutrals is defined by the Maxwell-Boltzmann relation $E_T = {}^3/_2 k_b.T$. In an applied field the kinetic energy is raised by $1/2M.v_D^2$. M is the molecular weight average (kg) of the ions and neutrals, which is effectively the average Molecular Mass of the neutral gas since the ion concentration relative to neutral carriers will always be very low (*i.e.* factions of 1%) and v_D is the ion drift velocity at the discrete applied field. Referring back to Section 1.2 it can been seen $v_D = K_{(E/N)}.E_D$, where $K_{(E/N)}$ is the high field mobility (m^2.V^{-1}.s^{-1}) and the energy (E_T) can therefore be redefined by Equation 17, where T is the ion temperature in the absence of the applied field.

$$E_T = \frac{3}{2}k_b T + \frac{1}{2}M.K_{(E/N)}^2.(E_D/N)^2 \qquad (17)$$

If it is assumed that ion to neutral collisions are elastic and the kinetic energy acquired in the applied field is retained in the velocity of the ion (in a dynamic equilibrium with its surroundings) the ion temperature will be raised to an *effective temperature, T_{eff}* (K) and the total energy to $E_T = {}^3/_2 k_b.T_{eff}$. Insertion of $E_T = {}^3/_2 k_b.T_{eff}$ into Equation 15 and factorizing terms, T_{eff} reduces to Equation 18.

$$T_{eff} = T + M.K_{(E/N)}^2.N_0^2.(E_D/N)^2/(3k_b) \qquad (18)$$

Polyatomic molecular ion clusters, however do not undergo elastic collisions because some of the kinetic energy is conserved and distributed amongst the rotational and vibrational degrees of freedom of the molecular ion. T_{eff} will subsequently be reduced by a factor ζ, *the ion-neutral collision efficiency factor* [1] -

$$T_{eff} = T + \zeta.M.K_{(E/N)}^2.N_0^2(E_D/N)^2/(3k_b) \qquad (19)$$

For ion clusters of molecular weights representative of volatile and semi-volatile chemicals (100 – 400g.mol^{-1}) factors of ~0.4 to ~0.7 are typical and applied fields of >80Td raise effective ion temperatures to many hundreds of Kelvin above the *neutral gas temperature* (*e.g.*, Figure 20). This may promote dissociation and fragmentation.
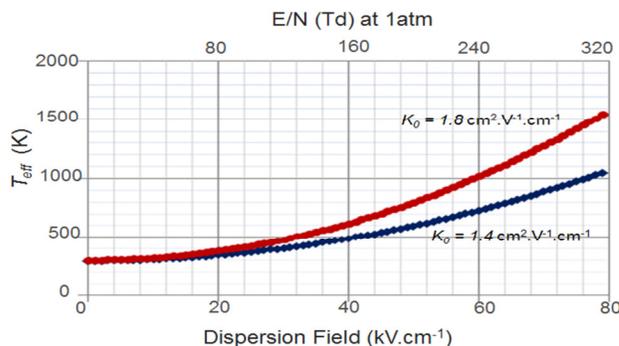

Figure 20: T_{eff} dependency on applied field for hypothetical ions of K$_0$ = 1.4 and 1.8V.cm^{-1}.s^{-1} and ζ = 0.5, at 1 atm. = 101.3kPa and a gas temperature of 50°C (323.15K)

Kinetic Processes in the Ion Filter

The residence time of an ion in the filter region is only a small fraction of that in the ionization region (which we define as the space between the ionizer and entrance to the ion filter). At very low E_D/N <10Td, where the effective ion temperature is only marginally higher than the gas temperature, ions with a lifetime exceeding the residence time in the Ionization region will remain intact on their traverse through the filter region. At increasing E_D/N however, ion reactions become kinetically favorable. Such processes may include; 1) dissociation of *ion-dipole (and ion-induced dipole)* bound solvating neutrals derived from the drift gas (*e.g.*, H$_2$O, N$_2$, *etc.*), 2) dissociation of proton bound species and 3) dissociation *via* the cleavage of a covalent site (*i.e.*, fragmentation). If E/N raises T_{eff} such to favor ion dissociation by one or more of these processes (on the timescale of ion residence time integrated across all high field segments of the Dispersion Field waveform) the conformation of the ion on exit from the filter will not match that on its entrance and the transmission model described in Section 3.2.1 cannot hold (because K_0 changes with the conformation of the ion). Citing the above dissociation processes, we can generalize that the dissociation energies order; 1 < 2 < 3, since an ion-dipole interaction is weaker than an ionic hydrogen bond and a covalent bond is stronger than an ionic hydrogen bond. At increasingly higher E_D/N (T_{eff}) these dissociation processes may be observed in the same order.

---

[1] It is important to note that the efficiency factor ζ is also a function of the gas temperature (T). This is discussed in Section 3. To simplify this initial analysis we assume it to be independent of T. In practice the gas temperature is fixed eliminating this variable (*i.e.*, such that it becomes wholly integrated within the empirically derived data).

To set the scene in this discussion we shall model the dissociation of the symmetrical proton bound dimer (M_2H^+), to a protonated monomer (MH^+) and neutral (M), as defined by the general reaction -

$$M_2H^+ \rightarrow MH^+ + M \qquad (20)$$

Under normal system operating conditions the concentration of M is << than other neutrals (the drift gas). The ion dissociates, as per Equation 20, during the high field portion of the waveform (when the ion is "hot") however, the probability of the reverse *association* reaction is negligible during the low-field period of the waveform (when the ion is "cool") because the probability of a monomer (MH^+) and neutral (M) collision is negligible on the timescale of the low-field period. Under these conditions, the rate (r, mol.s^{-1}) of dissociation can be defined by the first order rate law, where $[M_2H^+]$ is the concentration of dimer ions exiting the ion filter, t is time the dimer ion spends in the ion filter (s) and k is the first order rate constant (s^{-1}).

$$r = -d[M_2H^+]/dt = k[M_2H^+] \qquad (21)$$

At time = t the concentration of dimer ions in the ion filter $[M_2H^+]_t$ relative to the concentration of ions entering the filter at $t = 0$, $[M_2H^+]_0$ can be expressed by the integrated first order rate law –

$$[M_2H^+]_t = [M_2H^+]_0 \, \exp{-kt} \qquad (22)$$

and the first order rate constant (k) by -

$$k = -\ln[M_2H^+]_t/[M_2H^+]_0 \,.\, 1/t \qquad (23)$$

For the dimer cluster to make it through the separator and be detected its lifetime must exceed its residence time in the separator. Going a step further, for any dimer ions to be detected a finite proportion exceeding the level defining the signal to noise ratio of the system must remain undissociated on transit through the separation region. From Equation 23 the half-life of the dissociation process ($t_{1/2}$) will be given by –

$$t_{1/2} = \ln 2 / k \qquad (24)$$

The dimer dissociation rate constant k will exhibit some dependency on the molecule from which the dimer originates. Positive Ion Mode dimers are bound by an ionic hydrogen bond and typical binding energies range 90 - 130kJ.mol^{-1}, with dissociation rate constants <<1s^{-1} at STP. This delivers stability at lower Dispersion Fields, where the effective ion temperature (T_{eff}) is within a few 10's Kelvin of ambient (Figure 20) and many dimers therefore present themselves through the lower half of the E_D/N scan range (<150kV.cm^{-1}). However, k is extremely temperature dependent and at increasing E_D it may be expected that (D_T) tends to >> $t_{1/2}$, *i.e.* a vast proportion of dimer ions breakdown and the dimer response disappears.

To predict / interpret the breakdown field an understanding of the relationship of the effective ion temperature (T_{eff}) in relation to k is required. This is given by the *Arrhenius Equation* (Equation 25) in which R is the ideal gas constant (8.3145J.mol.K^{-1}), E_A the activation energy of dissociation (J.mol^{-1}) and A the Arrhenius constant (s^{-1}).

$$k(T_{eff}) = A. \, exp-\left(E_A / R.T_{eff}\right) \qquad (25)$$

E_A is related to the standard enthalpy of formation (-ΔH^o, J.mol^{-1}) which is the binding energy of the ionic hydrogen bond holding the dimer together through the expression $\Delta H^o = E_A + RT$, where T is standard Temperature (293.15K). For many proton bound dimers reference tables exist for ΔH^o, *e.g.* [14] and thus E_A is calculable. The Arrhenius constant (A, which is usually a very high power of e can be more difficult to look-up and very often this is derived empirically. There are, however examples that can be pulled out from the literature. Generally an approximation of log$A$ = 16.0 may be employed.

Case Example: Proton bound dimer of DMMP

log$A$ and E_A for the dissociation of the DMMP dimer are shown in Table 2. Substituting these values in Equation 25 we see (unsurprisingly) the dramatic exponential increase in dimer dissociation rate constant (k) over the T_{eff} range (~300 – 1200K) that correlates to the scanable E_D/N range of ~0 – 300Td at 1atm (for this DMMP dimer case). At ~160Td, $t_{1/2} \approx D_{T(H)}$ and at 180Td, $D_{T(H)}$ exceeds $t_{1/2}$ by >10.
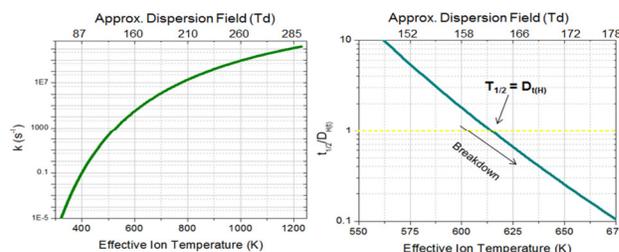

Figure 21: DMMP dimer dissociation rate constant (k) as a function of the effective ion temperature (T_{eff}) using LogA = 15.6s^{-1} and E_A = 127kJ.mol^{-1} (with T_{eff} calculated from Equation 19 using T = 318K and ζ = 0.72). Right: ratio of DMMP dimer half-life life (s) to integrated high field drift period in the ion separator ($D_{T(H)}$) of 13.5μs using $k(T_{eff})$ from left Figure.

The correlation between the thermal dependence of k and the ion transmission spectrum of the dimer will now become clearer. The ratio of dimer ions exiting the ion filter $[M_2H^+]_t$ to those entering it $[M_2H^+]_0$ can be determined from Equation 22 by replacing t with $D_{T(H)}$ and k with $k(T_{eff})$, where $k(T_{eff})$ is the dimer dissociation rate constant at the effective ion temperature in the high field portion of the applied waveform (*i.e.*, T_{eff} at E_D). This yields Equation 26, which ultimately defines the kinetic contribution to the shape function of the dimer Ion Transmission Spectrum (ITS).

$$[M_2H^+]_t / [M_2H^+]_0 = \exp{-k(T_{eff}).D_{T(H)}} \qquad (26)$$

Thus, where the dimer is stable in the ion separator, *i.e.* $k(T_{eff}).D_{T(H)}$ << $t_{1/2}$, a stable dimer response will be observed through the stepping of E_D (if losses to the filter electrodes due to diffusion defined in Equation 12 are neglected). However, at some point E_D raises T_{eff} such that $k(T_{eff}).D_{T(H)} \approx t_{1/2}$ and then readily such that $k(T_{eff}).D_{T(H)}$ >> $t_{1/2}$. With the exponential dependency of $[M_2H^+]$ / $[M_2H^+]_0$ on $k(T_{eff}).D_{T(H)}$ this drop off is dramatic (Figure 22)
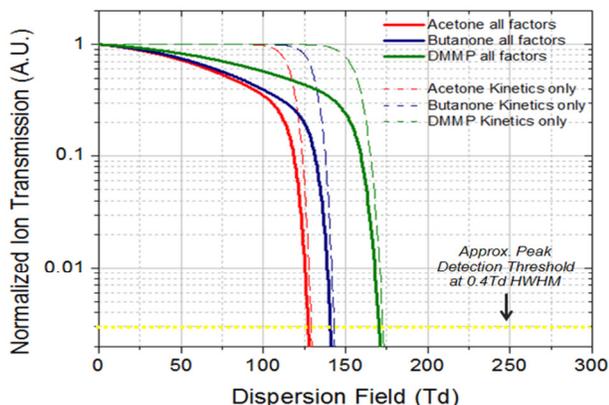
Figure 22: Dashed lines (----) predicted proton bound dimer ion transmission spectra at 1atm (where $[M_2H^+]_t$ / $[M_2H^+]_0$ is assumed proportional to ion current, *i.e.*, ignoring diffusional losses) for Acetone, butanone and DMMP using log A and E_A and ζ constants for (T_{eff} calculation) shown in Table 2 and gas temperature (T) of 318K. Solid bold lines (——) same predicted transmission spectra where diffusional losses are also accounted. K_0 values listed in Table 1 were used in all computations.

Case	LogA (s⁻¹)	E_A (KJ.mol⁻¹)	ζ (unitless)
Acetone	16.0	123.7	0.72
Butanone	16.0	124.7	0.72
DMMP	15.6	127.0	0.72

Table 2: Molecular constants used for dimer ion transmission models (Figure 21)

3.3 Peak Width

For a planar FAIMS / DMS separator the peak width ($W_{1/2}$) as Full Width at Half Maximum (*FWHM*), V.m⁻¹ is given by –

$$W_{1/2} = (4N/K_0 N_0).(D_{II} ln2/t_{res})^{1/2} \qquad (27)$$

where, t is the ion residence time (s) and the other terms have their previous meanings. D_{II} exhibits an E_D/N dependence by virtue of Equation 14 and thus so does the peak width. At constant pressure the $W_{1/2}(E_D/N)$ function evolves from near flat at lower E_D/N (<100Td) to quadratic at very high E_D/N (>300Td) (Figure 18.a). In the 0.5mm planar FAIMS topology exploited by Krylov *et al.* E_D/N operation was bounded in the 0 to 120Td range, meaning the effects of anisotropic diffusion on peak broadening were minimal (*i.e.*, the peak width could be assumed relatively constant through their operational E_D/N range). For the very high E_D/N operation employed by the present authors this is not the case. Equation 24 predicts an ~$W_{1/2}^{3/2}$ dependency on E/N (Figure 18.b).
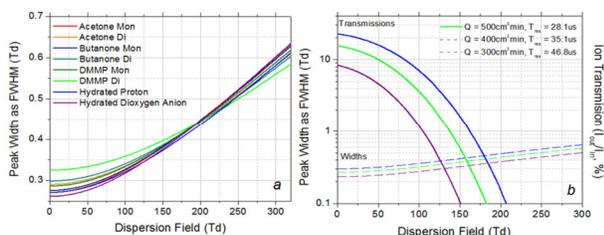

Figure 23: *a)* Computed $w_{1/2}(E_D/N)$ curves for product ions of differing K_0 (Table 1). *b)* Transmission and $w(E_D/N)$ curves (on the same scale) for the hydrated proton at different flow rates (ion residence times).

4 Validation and Discussion: Observed *vs.* Theory

The model discussed in the previous section is somewhat semi-quantitative. Limitations include, for example, the estimates one makes relating the various molecular ion constants (*e.g.*, ζ, k and A) and the approximation of $K_{E/N}$ for K_0 in T_{eff} calculations. These limitations can be qualified in an experiment *vs.* theory evaluation and we do so in this Section; examining the cases of Acetone, Butanone and DMMP cluster ions, as well as that of the Positive and Negative Ion Mode reactant ions (which we assume to be the hydrated proton and hydrated dioxygen anion, of general formula $H^+(H_2O)_n$ and $O_2^-(H_2O)_n$) . We choose these cases because they have been the subject of many IMS and DMS / FAIMS studies and many of the molecular ion constants defined in Equations 1 through 24 have been derived empirically. Acetone, Butanone and DMMP also yield relatively stable monomer ion clusters, enabling assessment throughout our working E_D/N range without the complication (in model evaluation) of ion fragmentation. In this particular evaluation we draw specific attention to the work of Krylov *et al.* [6, 9 & 16], Ewing *et al* [15] and Stone [17].

4.1 Experimental

Experimental conditions were set to replicate those employed by Krylov *et al.* described in [9]. Deviations from these conditions are explicitly highlighted.

4.1.1 Vapor Sample preparations and System Environmental Parameters

Acetone, Butanone and DMMP vapors were generated by PTFE incubated permeation sources. OVG-4 (Owlstone Ltd., Cambridge, UK) vapor generation systems equipped with outlet spit flow controls were used for permeation source incubation and manipulation of vapor level output. The vapor generator diluent gas was clean dry air output from a Zero Air generator passed over a 90A molecular sieve and activated carbon filter. PTFE source permeation rates were determined gravimetrically over an incubation period of 4 weeks. Acetone, Butanone and DMMP utilized in permeation sources was Analytical Standard grade, >99.9% purity (Sigma Aldrich, Poole, UK). The split flow output of the vapor generator was mixed with a clean dry air flow of the same standard as that fed into the vapor generator in order to manipulate the vapor level presented to the sensor platform. The gas flow rate through the sensor was 388 (±5) cm³.min⁻¹. This consisted of a 18cm³.min⁻¹ sample inlet flow and 370 cm³.min⁻¹ recirculating air flow. "At sensor" vapor levels studied ranged from 4 to 100ppb(V).

Pressure was monitored continuously at the output of the sensor assembly *via* the pressure sensor indicated in Figure 11 and logged with the output ion current data for later Td conversion. Sample humidity was monitored at the sensor outlet by means of a high precision Hygrometer (Cermet II IS, Michell Instruments Ltd, Cambridge, UK) and maintained <10ppm(V) H₂O for all experimental data reported herein.

4.1.2 Spectral Data Acquisition and Post Processing

$E_C:E_D$ spectra were generated with E_C drive settings of 401 data points in the –6V to –6V range and E_D settings of 51 points in the –

0 to 60V (V_b) range. This yielded 29.9mV E_C resolution and E_D 1.1V resolution respectively, equating to E_C/N of ~40mTd and E_C/N of 11Td at 1atm). Spectra were obtained in replicates of at least 20 over the course of 10 days. Raw spectra were processed off-line using a proprietary peak extraction algorithm, which reduced each raw spectrum to a set of Gaussian peak parameters (E_C/N, *Area* and *width*) at each E_D sample point in the scanned E_D/N range. Further post processing (graphical representation and mathematical processing) was performed using Microcal Origin version 6.0 (Microcal Software Inc., Northampton, MA).

4.2   Ion Peak Position

Krylov *et al*. [9] studied the field dependence of mobilities for the gas phase-protonated monomers and proton bound dimers of straight chain Ketones (of carbon numbers 3 to 10) in a dry air (~1ppm H_2O) drift gas, using a planar FAIMS system configuration described by Miller et al. [18]. The α_2 and α_4 parameters (Equation 5) for each ketone, under their experimental conditions, were determined with considerable precision (<5% LSD). In a separate publication [6] the same authors presented $E_C:E_D$ spectra and alpha plots for the DMMP monomer and dimer, as well as the solvated proton and solvated dioxygen anion (respectively the Positive and Negative Ion Mode reactant ions). This information offered the present authors with an opportunity for comparison utilizing the system described in Section 2.

In Figures 24 and 25 we compare empirically derived $E_C:E_D$ responses, for the above mentioned cases, with the theoretical, utilizing α_2 and α_4 coefficients quoted (or derived) from the above mentioned literature. In spectral representation we transpose Dispersion Field (the independent variable in Equation 9) to the Y axis and Compensation Field (the dependent variable in Equation 9) to the X axis, in convention with DMS / FAIMS standard for an intuitive spectral view (as illustrated in Figure 14). The sign of the Compensation Field axis is also reversed from that used in [6] and [9] to maintain convention with standard spatial representation of orthogonal axes. The *signs* of the α_2 and α_4 coefficients taken from [6] and [9] have therefore been reversed accordingly for this evaluation. Predicted responses have thus been modeled by means of Equation 9, using the α_2 and α_4 coefficients shown in Table 3 and our known $<f_2>$, $<f_3>$ and $<f_5>$ waveform coefficients (Section 2). Our experimental data has been fitted to the alpha model using only data in the lower half of the working E_D/N range (<140Td, or as specified on each graphic). Attempting to fit the alpha model across the entire range leads to a very poor fit since the alpha-model predicts $E_C/N \rightarrow E_D/N$ at high E_D/N (*c.f.* Section 3.1). Comparison of experimentally derived α_2 and α_4 coefficients at lower E_D/N with those published, nevertheless makes a useful point of reference in discussion. These derived α_2 and α_4 coefficients are also shown in Table 3.

Case	Krylov et. al [6, 9]		This work	
	α_2	α_4	α_2	α_4
Acetone (M)	-3.1 x 10^5	9.5 x 10^{-10}	-2.1 x 10^{-5}	1.2 x 10^{-9}
Acetone (D)	-1.3 x 10^{-5}	1.8 x 10^{-9}	-9.9 x 10^{-6}	1.1 x 10^{-9}
Butanone (M)	-2.7 x 10^{-5}	1.2 x 10^{-9}	-1.7 x 10^{-5}	9.7 x 10^{-10}
Butanone (D) [a]	-6.9 x 10^6	9.1 x 10^{10}	-6.6 x 10^{-6}	7.9 x10^{-10}
DMMP (M) [b]	-2.5 x 10^{-5}	2.5 x 10^{-9}	-7.7 x 10^{-6}	4.1 x 10^{-10}
DMMP (D) [b]	-3.8 x 10^{-6}	1.5 x 10^{-9}	7.2 x 10^{-7}	8.0 x 10^{-11}

Hyd. Proton [b]	-1.7 x 10^{-5}	2.6 x 10^{-11}	-2.5 x 10^{-5}	9.0 x 10^{-10}
Hyd. O$_2$ anion [b]	-2.3 x 10^{-5}	1.3 x 10^{-9}	-3.8 x 10^{-5}	2.7 x 10^{-9}

Table 3: a_2 and a_4 coefficients determined by Krylov compared with those obtained in this work. [a] *These Krylov values were derived from [9], (Figures 7 and 9 therein), since quoted values in Table 1 of that publication (p5443) do not support experimental the data that is presented.* [b] *These Krylov values were derived from data presented in [6] Figure 3.*

On first inspection Table 3 may seem alarming because of the marginal correlation between the comparative sets of α_2 and α_4 coefficients (a marginal correlation that is illustrated explicitly in Figures 24 and 25). However, it must be appreciated that the α parameters are very dependent on experimental conditions, in particular the ppm$_v$ water concentration at the sensor. Section 4.1 indicates that we were only able to roughly replicate the experimental conditions employed in [9]. It is the qualitative comparison that is of more interest *and critically* one must remember that chemical classification is based only partially on the $E_C:E_D$ profile in ion separations performed at Ultra-High Fields (as we shall discuss in Sections 4.3 and 4.4).
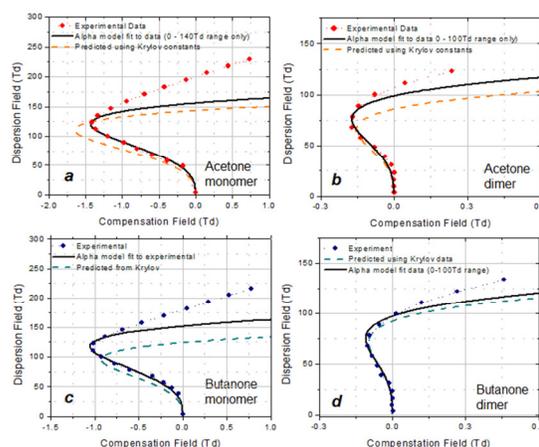

Figure 24: Experimental and predicted $E_C:E_D$ responses for Acetone and butanone. Experimental uncertainties in empirically derived Compensation Field values are < than the range captured within the area of the plotted data points (*i.e.*, <0.05Td).
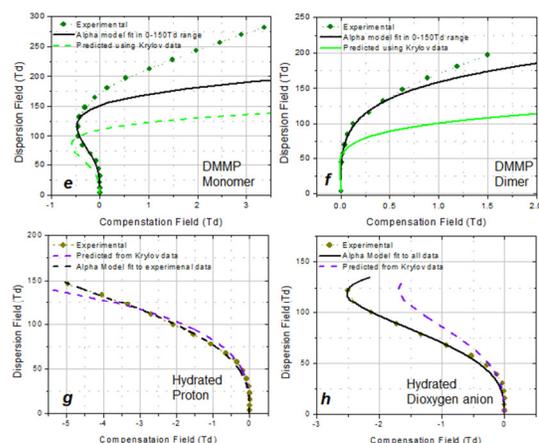

Figure 25: Experimental and predicted $E_C:E_D$ responses for DMMP and reactant ions. Again, Experimental uncertainties in empirically derived Compensation Field values are < than the range captured within the area of the plotted data points (*i.e.*, <0.05Td).

4.2.1   Acetone and Butanone

Qualitatively, the monomer and dimer responses of both acetone and butanone (comparing experimental data with the predicted responses) agree well at lower E_D/N range. For the monomers the alpha model fits well at E_D/N <140Td and for the dimers it fits well at E_D/N <100Td. At higher E_D/N the alpha model breaks down for both monomer and dimer as theorized. The monomer response extends to a considerably higher E_D/N than the dimer. The dimer response would be expected to decay in the mid E_D/N range because of field induced dissociation at the higher effective ion temperatures encountered in this mid E_D/N range. We shall discuss this further in Section 4.3. With respect to the deviation of the monomer response from the alpha model at higher E_D/N it may be accurately stated that at higher E_D/N the effective ion temperature in the lower field period of the applied waveform actually becomes appreciably higher than the gas temperature and that the approximation of the ion mobility to K_0 made in Equation 5 is no longer valid. For example, at a peak Td field of 200 the maximum Td field in the low field period reaches ~70Td. It may further be postulated that the model focuses too heavily on the physical process of the "solvation and desolvation" of neutrals. Whilst this is effective in the lower half of the E_D/N range (where effective ion temperatures are modulated only to within a few hundred K of the gas temperature) it may not be expected to be as effective at higher E_D/N, where effective ion temperatures become so high that that the ion cluster is entirely desolvated. This is discussed further in Section 4.3, since the Ion Transmission Spectrum provides additional information for this debate.

4.2.2   DMMP

The monomer and dimer responses of DMMP do not fit as well with the *Krylov et al.* predicted responses, although the alpha model still holds in the lower half of the E_D/N scan range. There was some uncertainty with respect to the experimental conditions used by Krylov *et* al. in [6] (ppm H_2O and gas temperature) and any mismatch in conditions would invalidate any comparison. Instead we focus on a comparison with our own acetone and butanone responses (shown in Figure 24). The gross observation for both the monomer and dimer cases are the much reduced -E_D/N of the turning point and extension of each response to a higher E_D/N. We interpret this in terms of the relatively larger collision cross sections of the monomer and dimer of DMMP (compared to their acetone / butanone counterparts), which is reflected in their lower respective ion mobilities (Table 1). Solvation / desolvation with neutrals thereby contributes less to the Differential Mobility between high and low field, reducing the negative E_D/N shift.

4.2.3   Reactant Ions

The reactant ions present in the lower half of the E_D/N scan range only. Transmission losses may be expected to attenuate the reactant ion signals at high fields because of their relatively high mobilities (*c.f.* Table 1 and Equation 12). The Positive Ion Mode reactant ion (which we assume here to be the hydrated proton) correlates very well with that predicted through the data of Kylov *et al*. [6], whereas the correlation with the Negative Ion Mode reactant ion (which we assume to be the hydrated dioxygen ion) shows some deviation. We consider the latter to be an artifact of the use of a corona ionization source by the present authors (as opposed to an Ni[63] ion source by the Krylov *et al.*). This hypothesis is

evaluated further by consideration of the Ion transmission and peak width (Sections 4.3 and 4.4).

4.3   Ion Peak Intensity & Ion Transmission

The Ion Transmission Spectrum (ITS), which we define as the integrated ion current of a resolved (or partially resolved) peak (as a function of E_D/N) is equally, if not more important for classification purposes, in Ultra High Field operation. Specifically the ITS is able to reveal information relating ion kinetics within the ion separator.

4.3.1   Reactant Ions

The Positive Ion Mode and Negative Ion Mode reactant ions (for which data was generated simultaneously) make for an easy study case, since in a clean system they present themselves wholly independently. The transmission spectra relating to Figures 25(c) and 25(d) and normalized to the transmission at E_D/N =0 are shown in Figure 26. The Ion transmission can be approximated to Equation 12 (with normalization eliminating pre-exponential factors), whereby the key parameter becomes K_0. Specifically, spectral interpretation requires consideration of $K(T_{tef})$. The Positive Ion Mode reactant ion seems the more straightforward of the two cases to explain. The transmission profile fits between that predicted for the $H^+(H_2O)_n$ of K_0 = 2.10 and 2.45 [10 & 13]. At increasing E_D/N the solvation number (*n*) of the cluster is expected to reduce and with this the ion mobility (*K*) increases.   The transmission profile transits from that for the cluster with the higher *n* (lower *K*) to that with lower *n* (higher *K*). The Negative Ion Mode response is less obvious. Under the experimental conditions the reactant ion would be expected to be either mono-hydrated [O_2^- (H_2O)] or de-hydrated [O_2^-], given the observations by Krylov *et al* [16]. However, neither K_0 fits the observed profile. A least squares fit of Equation 12 to the data yields a K_0 of 2.70 (±0.03) cm^2.V^{-1}.s^{-1}, which suggests a different Negative reactant ion (probably derived from the corona ion source). A Mass Spectral evaluation of corona ion chemistry has subsequently been undertaken and will be a subject of a separate article.
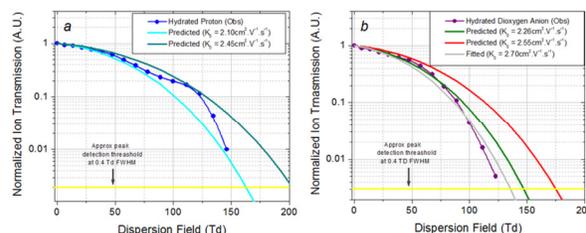

Figure 26: Positive (left) and Negative (right) Ion mode Reactant Ion transmission normalized to the integrated peak ion current at E_D/N = 0.

4.3.2   Dimers

A model for the dimer response was well established in Section 3.2. The experimental ITS for each of the three study cases are shown in Figure 27 with the predicted responses, combining diffusional and kinetic transmission losses overlaid.   Field dependent dimer breakdown is evident in the experimental data. The correlation between the experimental and predicted transmission spectra is not exact but this must be expected because of model approximations.   We summarize that the breakdown for butanone and acetone occurs at a lower than

predicted E_D/N, whilst that for DMMP occurs at higher than predicted E_D/N.

It was shown in Section 3.2 that the precise breakdown field of a dimer will be dictated by the effective ion temperature dependent first order rate constant $k(T_{eff})$ and the integrated high field ion residence time of the ion in the separation channel ($D_{T(H)}$) (c.f. Equation 26). In the case of acetone and butanone the $T_{eff}(E_D/N)$ profile is approximated due to lack of accurate knowledge of the ion-neutral collisional Efficiency Factor (ζ). Figure 27 suggests that this efficiency factor is likely overestimated. For the DMMP dimer the $T_{eff}(E_D/N)$ profile (which is shown in Figure 21) should be more representative since it has been experimentally derived by Ewing et al. [15]. One would expect therefore that the predicted and observed transmission profile should better correlate. Quantitatively there is a discrepancy of ~18Td between the predicted and observed breakdown field. The experimental data is too sparse to comfortably qualify this discrepancy but one may postulate that errors in the constants listed in Table 2 contribute, since they ultimately dictate the $T_{eff}(E_D/N)$ profile. Critically, the observed breakdown field is at least of the correct order.
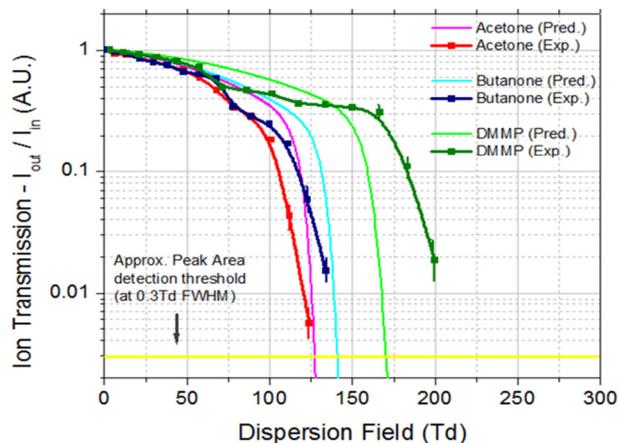

Figure 27: Normalized Ion transmission spectra for Acetone, Butanone and DMMP dimers. Experimental data point are indicted by dots with beta spline interpolation (•) where error bars are 1 standard deviation of the mean. Predicted responses are indicated with faint lines (——).

Whilst dimer breakdown is the prominent feature in the dimer ITS, transmission behaviors at E_D/N below the breakdown threshold should not be neglected. Below 100Td kinetic losses are negligible and the transmission is dictated wholly by Equation 12. Experimental observations in this lower E_DN region deviate from the predicted. Again, the experimental data is too sparse to comfortably qualify this discrepancy; however one may postulate that K_0 uncertainties in the $D_{ll}(E_D/N)$ computation are a contributory factor. A higher resolution study of the ITS would be beneficial to evaluate this.

4.3.3   Monomers

Acetone, butanone and DMMP monomers are thermally stable; that is they are not prone to fragmentation at a intramolecular covalent site, except at very high T_{eff} (~1000K). They are also relatively small molecules, so when thermally induced fragmentation does occur, the fragmentation products will be of low MW (and small collision cross-section). They will have a mobility >

than that of the parent ion.   On this basis one may presuppose that when the presence of dimer is suppressed (by keeping the vapor concentration at the sensor low) an ITS that strictly follows Equation 12 (and similar to reactant ions, shown in Figure 26) would be observed, since at fragmentation any fragment ions will exhibit diffusional transmission losses that exceed the ion detection threshold.   This hypothesis was tested by observing the ion transmission spectra of Acetone, Butanone and DMMP at sensor levels of 4ppp(v) - a vapor level that was found sufficiently low so as to reduce the dimer response to <1/5th that of the monomer response at the monomer dimer peak resolution point (~ 40Td). The results are shown in Figure 27.

Whilst there is some correlation between the observed and predicted ITS at lower E/N, there is an explicit lack of correlation at higher E/N.   Equation 12 predicts the transmission to decay exponentially with increasing E/N whereas the profile "valleys" (point A), "peaks" (point B) and then "decays" (point C) below the peak detection threshold on scanning through the 120 – 250 Td range. At point B the observed transmission exceeds the predicted by a factor >10^2.   Whilst this observation is bizarre and we are as yet unsure as to the precise physical process responsible for this effect, it is ultimately beneficial.   First, it delivers improved sensitivity in the mid E_D/N scan range and secondly the valley (A) and peak (B) points (as well as well as the end point C) exhibit molecular selectivity.   In respect of the latter, the monomer ITS delivers a useful classification feature.
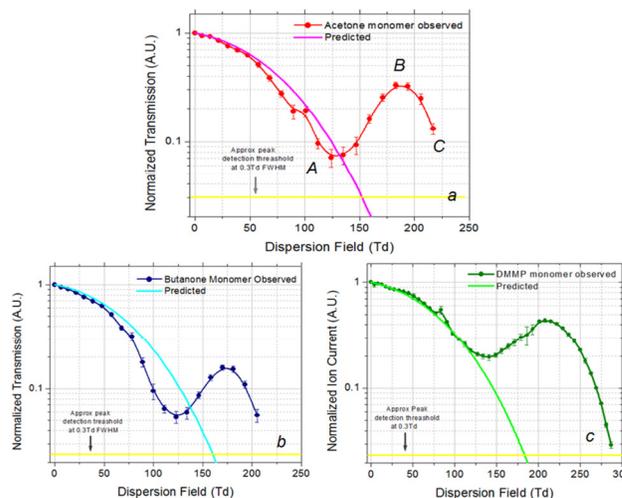

Figure 28: Monomer transmission spectra for a) Acetone, b) butanone and c) DMMP (data points • with beta spline interpolation) compared with theoretical responses (—— faint lines).

At higher vapor concentrations, where the dimer to monomer peak ratio is >>1 (in the lower E_D/N range) an ITS response of the form shown in Figure 28 may appear more rational.   At lower E_D/N the dimer will be dominant and the monomer suppressed. However, at mid E_D/N the dimer will breakdown and Equation 22 predicts this will result in an increase in monomer concentration within the ion filter. "Resurgence" in the monomer response would thereby be expected.   We can model this hypothesis and compare it with empirical data.

Below the dimer breakdown point we can denote the dimer concentration relative to the monomer concentration as $b.[M_2H]^+$

and that of the monomer $d.[MH^+]$, where b and d are the diffusion dependent transmission factors at E_D/N predicted by the exponent part of Equation 12. As the dimer breaks down the monomer concentration in the ion filter will become defined by-

$$[MH]^+ = d[MH]^+ + \left(d[MH]^+ . (1/b.x.[M_2H]^+) \right) \qquad (28)$$

where x is the fraction of dimer at $T_{eff}(E_D/N)$ predicted by Equation 26. Qualitatively Equation 28 predicts that the monomer ion transmission response will initially decay in the lower E_D/N range (according to Equation 12) until dimer breakdown starts occurring in the mid E_D/N range, whence it will rise again (since new monomer ions are formed within the ion filter). The response will then peak (once the dimer breakdown is effectively complete) before decaying again, from the peak point, in accordance with Equation 12.

In Figure 29 we assess this model against experimental data for acetone at a vapor concentration of $80(\pm10)$ppb$_{(v)}$ (whereby the dimer peak intensity at low E_D/N was observed to exceed the monomer by ~8:1). As expected the experimental data reveals a strong resurgence in monomer ion transmission (due monomer formation in the ion filter as the dimer breaks-down). However, the response does not properly correlate with that modeled by Equation 28. Instead, the monomer transmission response shows a shift to higher E_D/N (i.e., an improved transmission function) and the monomer peak response exceeds that predicted by a factor of ~2. These observations highlight deviations at high E_D/N from conventional ion models and further investigation is required in order to derive a physical explanation. This will be the subject of a future publication. For now, we can content ourselves with the conclusion that monomer ion transmission is more efficient than that predicted by Equation 12 and this ultimately delivers improved sensitivity through the higher end of the E_D/N range.
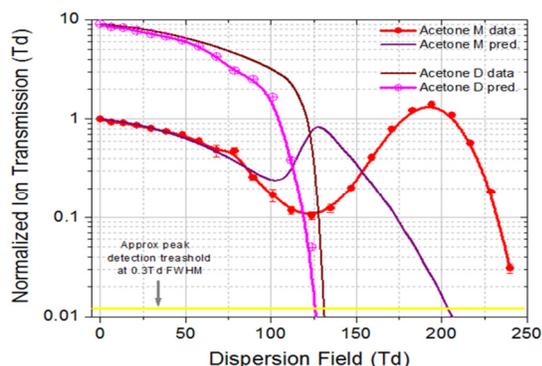

Figure 29: Observed and predicted ITS for the acetone monomer and dimer at 80ppb vapor concentration. Data has been normalized to the extrapolated monomer response at $E_D/N = 0$.

4.4 Ion Peak Width

Replacing D_{ll} in Equation 27 with *the Einstein Equation (Equation 15)* we may derive an expression that allows for the determination of K_0 from the peak width ($W_{1/2}$, V.m^{-1}) at zero E_D/N –

$$K_0 = \frac{16 N^2 N_0 ln2 . k_b T}{N_0{}^2 N . q t_{res} . W_{1/2}{}^2} \qquad (29)$$

On initial inspection this appears an attractive means by which to determine K_0 from the empirically derived $W_{1/2}$. However, there are two complications. First, there is of course no ion separation at zero field, so for species generating more than one ion, the zero field peak is a sum of the individual Gaussians. Secondly, the ion residence time must be accurately defined, which as we have seen in Section 2.2 is challenging since the flow velocity in the ion channel can only realistically be approximated to within a few percent in a rectangular micro-channel. We may nevertheless focus on a clean dry air sample and compare observed peaks for the hydrated proton and hydrated dioxygen anion with the theoretical prediction. We may go a step further and accurately derive the true ion residence time by substituting well referenced K_0 values for these particular air derived reactant ions.

4.4.1 Reactant Ions

We begin by looking at the experimental *vs.* predicted $W_{1/2}(E_D/N)$ responses for the reactant ions (Figure 30a). At low E_D/N (<50Td) a good correlation between predicted and theory is observed (when substituting the K_0 values shown in Table 1 into the Equation 27). We observe just a small, relatively constant offset of 0.02 Td between experiment and theory. If it is assumed that the ion residence time is accurately defined, it may further be assumed that this is due to a discrepancy between the actual K_0 and that input in the model. Extrapolating the observed $W_{1/2}(E_D/N)$ data points in the 0 – 50Td range to zero (Figure 30b), we obtain a zero Td $W_{1/2}$'s of 0.2738 ($\pm$0.0013) for the hydrated dioxygen anion and 0.2738 ($\pm$0.0013) and 0.2883 (0.0010) for the hydrated proton. Feeding these values into Equation 29 yields a K_0 of and 1.99 ($\pm$0.01) cm^2.V.s^{-1} and 1.80 ($\pm$0.01) cm^2.V.s^{-1} for the respected cases (compared to their literature values of 2.26 and 2.10 cm^2.V.s^{-1}). One would conclude from this (assuming our reactant ion identities are correctly assigned) that the ion residence time is not acutely defined.

If the reverse problem is solved and the literature quoted K_0 values are used in combination with the zero Td extrapolated experimental $W_{1/2}(E_D/N)$ data, in order to obtain the ion residence time, one obtains t_{res} = 31.9 ($\pm$0.2) µs for the hydrated dioxygen anion and 30.9µs ($\pm$0.2) for the hydrated proton. This compares to a computed ion residence time at the working flow rate (388cm^{-3}.min^{-1}) of 36.9µs. It may seem that a further analysis of the micro-channel gas flow is warranted. However, it must not be neglected that the ion transmission spectra (Figure 26) would not correlate as well under the assumption of a shorter Ion residence time (since Ion transmission would increase). It seems more likely that there is an additional factor that broadens the peak.
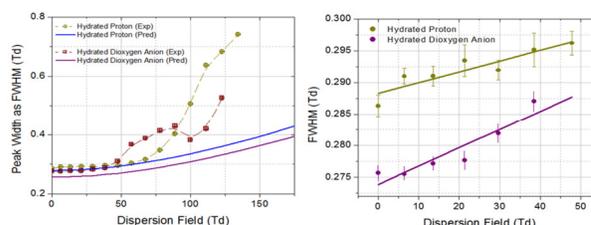

Figure 30: a) Observed and predicted $W_{1/2}(E_D/N)$ profiles for the positive ion mode and negative ion mode reactant ions (of assumed identity given in Table 2). b) Experimental data observed in the 0 – 50Td range, where the Error bars are standard deviations (n = 20).

Moving on to consider the $W_{1/2}(E_D/N)$ response at higher E_D/N we observe a considerable deviation from experiment and theory. $W_{1/2}(E_D/N)$ does not evolve smoothly and begins to exceed the predicted $W_{1/2}$ appreciably (> twice the predicted $W_{1/2}$ at ~110Td). The additional broadening may be attributed to 2 factors. First, we may be running into a situation whereby we have an assembly of ions of differing hydration number - $(H_2O)_n$. The reactant ions are very small and have high K values >2.1cm^2.V^{-1}s^{-1}. Any change in hydration number will have a large impact on K and the ion assembly will become "partially" resolved into its $\Delta K(E_D/N)$ elements. However, the resolution is not sufficient for the peak extraction algorithm to pick out the peaks and they become integrated as a single broad peak. The second aspect is that at increasing field the ion is driven toward desolvation (dissociation of the ion-dipole bound water neutral). Near the dissociation point the collision cross-section of the ion increases disproportionally (particularly for small cluster ions) and K undergoes a rapid decrease over a narrow E_D/N range. This broadens the peak by virtue of Equation 27.

4.4.2 Monomers and Dimers

Whilst, for the monomer and dimers it is not possible to effectively evaluate the $W_{1/2}(E/N)$ response at very low E_D/N (<50Td) due to marginal peak resolution, it is informative to study the response at higher E_D/N where the peaks are fully resolved. The observed and predicted responses for the monomers / dimers are shown in Figure 31. At lower E_D/N (<130Td) experimental and predicted data does correlate well. At higher E_D/N an increasing deviation from the predicted is observed. In the case of the dimer the observed $W_{1/2}(E/D)$ tends exponential around the breakdown field. The monomer response is more stable but shows unusual features (turning points similar to those observed for the hydrated dioxygen anion). They may be related to the K variations invoked through field induced desolvation. Ultimately a higher resolution study is required to fulfill understanding here. However, it should be appreciated that these turning points can be expected to be ion specific and therefore of use in classification.
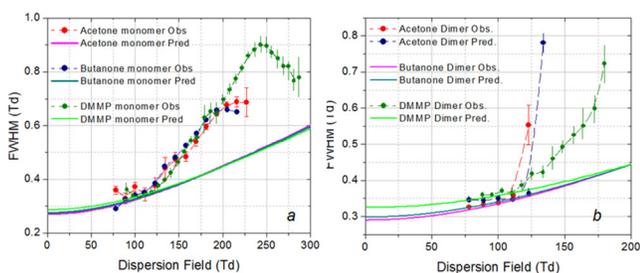

Figure 31: a) $W_{1/2}(E/N)$ responses for acetone, butanone and DMMP monomers (data points • with beta spline interpolation) compared with prediction (lines ——). b) Dimer responses. Errors are standard deviations (where for acetone and butanone n = 20, for DMMP n = 5).

5 Conclusions and Forward

This paper draws attention to differences in the operational models applied in conventional lower field range DMS / FAIMS systems as compared to a system that operates over a significantly higher field range. The system described has been evaluated over a field range of 0 – 300 Td, nearly *trebling* the field range explored in

previously described systems. The key aspect of higher field operation is the non-linear dependency of effective ion temperature on operational field. *Trebling* the operational field increases the effective temperature range over which an ion can be studied by as much as a factor of 9 because of the ~$T_{eff} \propto E_D/N^2$ dependency. This has profound benefits, since the high effective ion temperatures lead to the fragmentation of ions within the ion filter and these fragmentations exhibit field dependent specificity by virtue of their unique kinetic and thermodynamic constants. FAIMS / DMS models fail to represent ion separations adequately and a new *Rapid Thermal Modulation Ion Spectrometry* (RTMIS) terminology serves more appropriately.

It is appreciated that *ab inito* spectral modeling at Ultra-High fields it complicated by uncertainties in molecular ion constants, in particular the ion-neutral collision Efficiency factor (ζ) and kinetic parameters that dictate fragmentation (*e.g.*, the Arrhenius constant A and the effective ion temperature dependent rate constant $k(T_{eff})$. In practice empirical training delivers data in which these constants are wholly integrated and critically, a mature, well characterized system solution has been described that can allow this training data to be generated with considerable confidence.

References

[1]   E. A. Mason, E. W. McDaniel, Transport Properties of Ions in Gases, Wiley, New York, (1988)

[2]   G. A. Eiceman & Z. Karpas, Ion Mobility Spectrometry, CRC Press, Boca Raton (2005)

[3]   A. A. Shvartsburg, Differential Ion Mobility Spectrometry, CRC Press, Boca Raton (2009)

[4]   E.G. Nazarov, S. L. Coy, E. V. Krylov, R. A. Miller, G. A. Eiceman, Pressure effects in differential mobility spectrometry, *Anal Chem.* **78** (2006), 7697-706.

[5]   A. A. Shvartsburg, R. D. Smith, A. Wilks, A. Kohel, D. Ruiz, B. Boyle; Ultrafast Differential Ion Mobility Spectrometry in Multichannel Microchips, *Anal. Chem.* **81** (2009), 6489-6495

[6]   E. V. Krylov , E. G. Nazarov, R. A. Miller, Differential mobility spectrometer: Model of operation, *Int. J. Mass Spectrom.*, **266** (2007), 76–85

[7]   A. Tamayol, M. Bahrami; Laminar Flow in Microchannels with Noncircular Cross Section, *J. Fluids Eng.*, **132** (2010), 111201-1 − 111201-9

[8]   R. Guevremont, High-field asymmetric waveform ion mobility spectrometry: A new tool for mass spectrometry, *J. Chromatogr. A*, **1058** (2004), 3–19

[9]   *E.V. Krylov, E. G. Nazarov, R. A. Miller, B. Tadjikov and G. A. Eiceman;* Field Dependance of Mobilities for Gas-Phase-Protonated Monomers and Proton-Bound Dimers of Ketones by Planar Field Asymmetric Ion Mobility Spectrometry (PFAIMS), *J. Phy. Chem. A.*, **106** (2002), 5547 − 5444)

[10] W. Vautz, B. Bödeker, J. I. Baumbach, S. Bader, M. Westhoff and T. Perl; An implementable approach to obtain reproducible reduced ion mobility, *Int. J. Ion Mobil. Spectrom.* **12** (2009), 47 − 57.

[11] H. Bensch & M. Leonhardt, Comparison of Drift Times of Different IMS, *Int. J. Ion Mobil. Spec*trom., **3** (2002), 7 − 10.

[12] M. Tabrizchi and F. Rouholahnejad; Comparing the effects of Temperature and Pressure on Ion Mobility, 2005 *J. Phys. D: Appl. Phys.* **38** 857

[13] H. E. Revercomb, E. A. Mason; Theory of plasma chromatography/gaseous electrophoresis. *Anal. Chem.*, 1975, **47** (7), 970–983

[14] National Institute of Standards web book page (and literature references therein - http://webbook.nist.gov/cgi/cbook.cgi?ID=B5000324&Mask=8

[15] R. G. Ewing, G. A. Eiceman, C. S. Harden, J. A. Stone, The kinetics of the decompositions of the proton bound dimers of 1,4-dimethylpyridine and dimethyl methylphosphonate from atmosphere pressure ion mobility spectra, *Int. J. Mass Spectrom.* **76** (2006), *255-256*

[16] E. V.. Krylov, S. L. Coy, and E. G. Nazarov, Temperature effects in differential mobility spectrometry, *Int. J. Mass Spectrom.*, **279** (2009), *119-125*

[17] J. A. Stone; The Kinetics and Thermodynamics of Ion Solvation Applicable to Ion Mobility Spectrometry, *Int. J. Ion Mob. Spectrom.* **5** (2002), *19 – 41*

[18] E. Krylov, E.G. Nazarov, R.A. Miller, B. Tadjikov, and G.A. Eiceman, Micromachined Planar Field Asymmetric Ion Mobility Spectrometer, *Sensors Actuators A.*, **91** (2001), *301-312.*

Acknowledgements